Atomic Force Microscopy-Based Two-dimensional Infrared Nano-spectroscopy

Qing Xie, 1 Yu Zhang, 2 Eli Janzen, 3 James H. Edgar, 3 and Xiaoji G. Xu1*

¹Department of Chemistry, Lehigh University, 6 E Packer Ave. Bethlehem, Pennsylvania, 18015, United States

²Ames National Laboratory, Iowa State University, Ames, Iowa 50011, United States

³Tim Taylor Department of Chemical Engineering, Kansas State University, Manhattan, Kansas 66506, United States

*Email: xgx214@lehigh.edu

For decades, infrared (IR) spectroscopy has advanced on two distinct frontiers: enhancing spatial resolution and broadening spectroscopic information. While atomic force microscopy (AFM)based IR microscopy reaches sub-10 nm spatial resolutions, overcoming Abbe's diffraction limit, time-domain two-dimensional IR spectroscopy (2DIR) provides unparalleled insights into molecular structures, mode coupling, and energy transfers. These two realms, however, evolved separately. Here, we bridge their boundary by introducing the AFM-2DIR nano-spectroscopy that offers the spatial precision of AFM with the rich spectroscopic information of 2DIR. This innovative approach utilizes the mechanical detection of the sample's photothermal responses from a tip-enhanced femtosecond IR pulse sequence. We demonstrate it on the carbonyl mode, elucidating its anharmonicity. Further, leveraging near-field photons' high momenta from the tipenhancement for phase matching, we photothermally probe hyperbolic phonon polaritons in isotope-enriched h^{-10} BN. Our measurement confirms energy transfers between phonon polaritons and phonons as well as among polariton modes, possibly aided by scattering at interfaces. The AFM-2DIR nano-spectroscopy enables in situ investigations of vibrational anharmonicity, coupling, and energy transfers in heterogeneous materials and nanostructures, especially suitable for unraveling the relaxation process in 2D materials in IR frequencies.

Under light illumination, the sharp metal-coated tip of an atomic force microscope (AFM) localizes and enhances the optical field underneath its apex. The spatial scale of the field enhancement is comparable to the nanoscopic tip radius and is effectively wavelength-independent. Capitalizing on tip enhancement, innovative AFM-based super-resolution infrared (IR) imaging tools have been developed. Notable among these are the scattering-type scanning near-field optical microscopy (s-SNOM) with optical detection¹⁻³ and AFM-IR microscopy with photothermal mechanical detection.⁴ Furthermore, photons from the tip enhancement possess high spatial frequencies and carry much higher momenta than free-space photons, which have been utilized to launch phonon polariton (PhP) in low dimensional materials in the mid-IR frequency.⁵ The AFM-based imaging tool has been instrumental in studying polaritons in 2D materials.⁶⁻¹²

Among the broad range of the electromagnetic spectrum, IR radiation is popular for spectroscopy because it matches transition frequencies of vibrational modes and usually has a stronger cross-section than Raman. One frontier of IR spectroscopy is the time-domain two-dimensional IR (2DIR), which scans a time-controlled sequence of femtosecond IR pulses ¹³⁻¹⁵ to deliver rich spectroscopic information, revealing anharmonicities, coupling, and energy transfer. ^{16, 17} However, 2DIR is usually restricted by Abbe's diffraction limit, which leads to poor spatial resolution.

Integration of AFM's tip-enhancement with 2DIR would overcome Abbe's diffraction limit, enabling the spatial resolution to reach the nanometer scale. However, despite steady progress in AFM-based time-resolved pump-probe near-field spectroscopy in the realm of s-SNOM with optical detection, ¹⁸⁻²⁴ the integration of AFM with 2DIR remains under-explored. Here, we integrate the photothermal AFM-IR detection with 2DIR to form a new nano-spectroscopy method. Compared with s-SNOM, the AFM-IR detection approach to 2DIR has low instrument complexity by avoiding interferometric photon detections. It also has the advantage of directly probing the energy dissipation due to IR absorption, rather than the collective polarizability of the tip-sample junctions. The resulting AFM-2DIR employs a sharp metallic AFM tip to mechanically detect the photothermal response of a sample triggered by a tip-enhanced femtosecond IR pulse sequence. The relative timings between the IR pulses in the sequence are systematically scanned, and the corresponding modulations in photothermal signals are recorded and extracted via 2D Fourier transform (FFT). As a demonstration, we employed this method to uncover the anharmonicity of the carbonyl vibrational mode and to elucidate the possible energy transfer pathways of PhP in hexagonal boron nitride (*h*-BN).

A detailed construction of the apparatus is described in the Methods section. In short, the AFM-2DIR apparatus (Fig. 1a) consists of three main components: generation of a femtosecond IR pulse sequence, an AFM with a metallic tip, and a photothermal signal extraction mechanism. In our setup, we utilize a temperature-regulated compact assembly of Michelson interferometers (marked by the dashed box) to generate a collinear, time-controlled sequence of three pulses, with t₁ and t₂ to represent the time separations between adjacent pulses. A parabolic mirror focuses the IR pulse sequence at the AFM tip. The timing t₁ and t₂ are scanned during the measurement while recording photothermal signals. The photothermal signal is generated and extracted following the mechanism of the peak force infrared (PFIR) microscopy. PFIR is an emerging AFM-IR technique with <10 nm spatial resolution and works well with low repetition light source. ²⁵ The AFM is operated under peak force tapping (PFT) mode, in which the AFM tip intermittently and predicably contacts the sample surface, to which the IR emission is synchronized (Fig. 1b). The tip-enhanced pulse sequence excites the sample's IR resonances, followed by relaxations in the picosecond time scale to generate heat. Rapid thermal expansion of the sample in the sub microsecond scale exerts an impulsive force and excites AFM's cantilever to oscillate at hundreds of kHz (Fig. 1c), which is read out through the cantilever vertical deflection signal from a built-in quadrant photodiode. FFT retrieves the amplitude of the cantilever oscillation, which is integrated in a frequency window and used as the photothermal signal S (Fig. 1d).

The collective absorption of the IR pulse sequence and subsequent non-radiative decay contributes to the photothermal signal. The time separations t_1 and t_2 between the pulses in the sequence influence which states and how they are populated, causing modulations in the photothermal signal. In simple spectroscopy terms, the first two pulses are considered as the pump. The temporal separation t_1 determines which subset of IR frequencies within the IR bandwidth is utilized to populate vibrational states. The third pulse acts as the probe, the absorption of which is modified by existing excited states prepared by the pump. The excited state populations after the collective interactions of the pump and probe give rise to the photothermal signal after relaxation. The timing t_2 between the second and third pulse determines the frequency component to be probed. More complex light-matter interaction pathways beyond linear IR absorption, such as the excited state absorption, mode coupling, and energy transfer are affected by the timings of t_1 and t_2 of the pulse sequence, thus embedded in the modulation of the photothermal signal S. Sequentially performing FFTs on $S(t_1, t_2)$ recovers a 2D spectrum of $S(\omega_1, \omega_2)$ in the frequency domain. Fig. 1f shows a spectrogram $S(t_1, \omega_2)$ from FFT of $S(t_1, t_2)$ along the fast scan axis of t_2 . Additional FFT is performed along t_1 on the real part of $S(t_1, \omega_2)$ to obtain $S(\omega_1, \omega_2)$. We name $S(\omega_1, \omega_2)$ the 2D PFIR spectrum, as it is obtained by the PFIR detection mechanism.

Results

Revealing anharmonicity of carbonyl vibrational mode

The 2D PFIR spectrum is usually complex-valued from the 2D FFT. The absolute value of the 2D PFIR spectrum of carbonyl vibrational modes from a 50 nm thick PMMA-N₃ polymer film is plotted in Fig. 1g. We can discern excited state absorption from the extended tail along the lower frequency of ω_2 . A more informational visualization of a 2D PFIR spectrum is to present its real part. Fig. 2a shows the real part of Fig. 1g (the imaginary part is included in Supplementary Figure S1a). This 2D spectrum resembles the optical-detected 2DIR spectrum of a carbonyl vibrational mode of homogeneously broadened profile, which can be understood by the fact that the AFM tip only probes a nanoscopic region of the sample that suffers much less spatial averaging than the far-field 2DIR. Both ground state depletion and excited state absorption, denoted as $(0 \to 1)$ and $(1 \to 2)$ respectively, are present. Additional spectral signatures showing successive overtone absorptions, such as $(2 \rightarrow 3)$ are also observed. The anharmonicity Δ is revealed by the energy separation between $(1 \rightarrow 2)$ and $(2 \rightarrow 3)$ to be 19 cm⁻¹, which is slightly larger than typical carbonyl modes.²⁶ However, this value is consistent with our previous tip-based frequency-domain pumpprobe PFIR experiment based on quantum cascade lasers (QCL).²⁷ Also, we found that the time-domain 2D PFIR spectrum of the carbonyl of PMMA-N₃ exhibits noticeable different shape for a higher incident laser power (Fig. 2c), which is likely caused by the strong field strength and second-order gradient of electric field of the tip enhancement. We discuss its possible origin in the Supplementary Note 1 and Fig. S2.

To understand the signal generation mechanism, we schematically illustrate a vibrational potential energy surface (PES) and three representative Feynmann diagram pathways in Fig. 2b that correspond to the spectroscopic features. Because the photothermal signal is based on heat generation from the relaxation of populations of excited states, corresponding pathways of Feynman diagram should involve a corresponding "population" term, *i.e.*, |n>< n|, where n represents an excited vibrational state (n>0). For instance, the spectral feature of $(1\to 2)$ is generated when the state |1> is created by the first and the second IR pulses, denoted as i and ii, and then |2> is formed by the second and third pulses, labeled as ii and iii. The decays of the populations at |1> and |2> generates photothermal signal. Since the level |2> has a higher energy than level |1>, it generates more heat when relaxed, making the $(1\to 2)$ a positive feature. Likewise, $(0\to 1)$ is a negative feature since the probe converts |1> into |0>, reducing the population of excited states. The overtone of excited state absorption $(2\to 3)$ is generated by the first pulse interacts with sample two times (i and i) to prepare the population in |1>, and follow by a similar ladder climbing pathways.

Note that generating the photothermal signal requires the population of excited states during or after the IR pulse sequence. The polarization-only or coherence-only Feynman diagram pathways, which contribute to certain channels of four-wave-mixing signal, should not contribute to the photothermal signal as they do not generate population. This characteristic could be a difference between photothermal AFM-2DIR versus optical-detection 2DIR approach, including an s-SNOM based 2DIR, if it were to be developed.

Probing energy transfers of PhP in h-10BN by AFM-2DIR

h-BN is a 2D material that supports hyperbolic PhP,^{6, 28-30} which travels within the material with high momentum and low energy in the IR. Due to the restriction from phase matching condition, PhP in *h*-BN cannot be efficiently generated by far-field IR illumination. Instead, they are usually studied by the tip-based IR s-SNOM,^{6, 21, 28, 30-35} and to less extent, AFM-IRs.^{36, 37} These AFM-based imaging tools visualize the spatial distributions of interference fringes resulting from standing waves of propagating PhPs launched by the tip site and edge reflections back to the tip.

While hyperbolic PhP (HPhP) has immense potential for nano-optical applications of optical energy delivery,^{35, 38} subwavelength imaging,³⁰ and chemical sensing,³⁹ gaps remain in the understanding of their relaxation process. Broadly speaking, relaxation involves energy transfers from initial excited states or resonances to other degrees of freedom, eventually becoming heat. When the direct radiative decay is limited, the principal dissipation route of PhPs is believed to be through non-radiative phonon scattering, *i.e.*, interactions with phonons in the lattice that facilitate energy transfer.^{40, 41} However, the experimental tool to directly probe energy transfer among the phonon and PhP modes is absent. Our technique, the photothermal AFM-2DIR spectroscopy, seeks to fill this gap.

When the AFM tip illuminated by IR is in contact with h-BN, the tip-enhanced field launches PhPs. In our experiments, we studied isotope-enriched h- 10 BN, which possesses stronger PhP responses than natural h-BN and has become a standard sample for polariton research. $^{33,42.46}$ We first perform the single-frequency PFIR microscopy on a flake of h- 10 BN with a QCL as light source to verify the presence of PhPs. The description of the regular PFIR setup is included in the **Methods**. Fig. 3a displays the AFM topography of an h- 10 BN flake with 40 nm thickness (read out in Supplementary Figure S3). Fig. 3b-f are the progression of interference fringes of PhPs under different IR frequencies. These interference fringes are similar to those observed by s-SNOM. 6,32 However, PFIR signal originates from photothermal response, i.e., heat dissipation of absorbed IR photons by the tip-sample junction. When the tip-launched PhP traverses an integer multiple of 2π in phase and return to the tip, a standing wave cavity is formed, enhancing IR absorption and eventually leading more heat generation. We extract the spatial frequencies of interference fringes through FFTs (Fig. 3g). A positive correlation between IR energy and the spatial frequencies is observed, which is a manifestation of the energy-momentum dispersion relation of propagating PhP supported by this h- 10 BN flake. 6,32

What determines the bandwidth of the available momenta for launching PhPs? We perform the finite element simulation on the IR field distribution for a conical Pt tip of a half sphere apex above a h-BN layer of ~40 nm thickness. Fig. 3h displays the sectional profile the EM field amplitude. The amplitude at the tip-sample junction is enhanced and confined to a spatial scale smaller than the tip radius. A FFT of the spatial field distribution at the sample surface yields the bandwidth of momentum for the near-field photons (Supplementary Figure S4). In Fig. 3i, we overlay the estimated IR bandwidth from our IR source and momentum from finite-element simulation with the simulated dispersion relation of HPhP of h- 10 BN of the same thickness. The experimentally extracted momentum versus IR frequency pairs from Fig. 3g are overlaid as discrete points. The simulation follows description in literature $^{6, 32}$, details can be found in **Methods.** The overlap indicates multiple polariton modes are accessible by the combined bandwidth of energy and momentum. High optical density of states is present right above the h- 10 BN's phonon resonance at ~ 1390 cm $^{-1}$, where the dispersion relations of multiple PhP modes (m = 0, 1, 2...) start (dashed line in

Fig. 3i). At higher IR energy above 1420 cm^{-1} , only the first a few modes (m = 0, 1) are accessible from the energy-momentum bandwidth of our tip enhancement.

Fig. 4 displays the 2D PFIR measurement of the h- 10 BN flake. We performed measurements on two locations 1 and 2, marked on the AFM topography (Fig. 4a). They are located 200 nm and 1500 nm from the left edge of the flake, respectively. The point spectra from Fourier transform PFIR (FT-PFIR) spectroscopy displayed in Fig. 4b are acquired by scanning the time separation of only two IR pulses and perform FFT on the interferogram from photothermal signal. The detailed procedure FT-PFIR is described in literature. ⁴⁷ Three main peaks are observed from the FT-PFIR spectrum around 1405 cm⁻¹, 1420 cm⁻¹ and 1440 cm⁻¹. Direct photothermal response from the optical phonon at 1390 cm⁻¹ is found to be weaker than PhP responses, likely due to the long axis of the metallic tip for field enhancement being perpendicular to the in-plane phonon mode and the IR excitation was centered at 1415 cm⁻¹. The 2D PFIR measurements were performed by scanning t_1 and t_2 to collect series of interferograms. The spectrogram of $S(t_1, \omega_2)$ of Location 1 is presented in Fig. 4c, which exhibits a decay trend on the interference contrast along t₁. The real part of the 2D PFIR spectra from two locations are displayed in Fig. 4d and 4e (real part 2D PFIR spectrum from a location at 800 nm from the left side edge is plotted in Supplementary Figure S5). The absolute value and imaginary parts of the same spectra are included in the Supplementary Figure S6. The overall spectral profile of h-10BN is significantly different from that of carbonyl because HPhPs are propagating waves travel within the $h^{-10}BN$ flake, whereas the carbonyl vibrational modes are local to molecules and do not propagate like a wave.

The 2D PFIR spectra (Fig. 4d and 4e) exhibit both diagonal features and off-diagonal features. To facilitate discussion, we label the features with numbers (1 to 7) in Fig. 4d. The diagonal features (1, 2, 3) correspond to the excitations that are accessible by IR frequencies. The sectional feature of the diagonal peaks resembled the spectral peaks obtained from the linear FT-PFIR spectra of Fig. 4b, a correspondence that is expected by 2DIR spectroscopy. Feature 1 can be attributed to the cluster of polariton modes (m = 0, 1, 2,...) right above the h^{-10} BN phonon frequency of 1390 cm⁻¹. These modes exhibit a wide range of momenta but close in energy. In another word, this energy region has a high density of polariton modes that can be populated by the near-field photons of similar energies. Feature 2 arises from m = 1 mode. It appears weak, because m = 1 mode has smaller PhP wavelength than m = 0 mode and higher propagation loss per unit length. Feature 3 is from m = 0 mode at a higher frequency, representing a standing wave mode from the edge of the h^{-10} BN flake. Features 2 and 3 are greatly suppressed in Fig. 4e, because the tip was placed 1.5 um from the flake edge during the measurement. Propagation loss over a long range reduces the quality of standing wave mode at higher IR frequencies.

What causes the off-diagonal responses? Generally, an off-diagonal feature at a frequency pair of (ω_1, ω_2) suggests that the light-matter interaction of photons at ω_2 (pump) modifies the light-matter interaction of photon at ω_1 (probe). Energy transfer usually implies that the state of origin has to be populated before the target state, *i.e.*, satisfying causality, which is manifested in 2DIR spectra as asymmetric off-diagonal features.^{17, 48} In our measurement, four off-diagonal features (4, 5, 6, and 7) are observed from Fig. 4d; two features (4 and 5) are observed from Fig. 4e. All of them are asymmetrically positioned, which indicates their generations involve energy transfers pathways.

What is the possible origin for feature 4 in the 2D PFIR spectra? This feature has a pump at 1405 cm⁻¹ and probe at 1390 cm⁻¹. This energy transfer pathway can be interpreted as the energy transfer from the collection of high density PhP modes right above the phonon mode to the phonon mode itself—the usual destination of PhP relaxation. The phonons at 1390 cm⁻¹ are populated from this energy transfer pathway, and the net absorption of the probe photon at its phonon frequency is reduced, akin to the relationship between absorption and stimulated emission. Thus, this energy transfer pathway is manifested as a negative feature in the 2D PFIR spectra. Similarly negative but weaker features (marked by an arrow in Fig. 4d) are observed between phonon frequency and phonon polaritons of features 2 and 3 suggesting

similar pathways. This conversion from PhPs to phonons happens through phonon scattering, which is always present and independent of the tip position.

Feature 5 exhibits a positive feature and suggests the energy transfer is from the collection of PhP modes at 1405 cm⁻¹ to PhP modes centered at 1427 cm⁻¹. The feature's horizontally elongated profile suggests a collection of modes are involved. How do we understand the energy transfer pathways among PhP modes? Energy transfer usually requires two resonances to spatially overlap, or at least, to be spatially close. However, HPhPs in *h*-BN has a characteristic property that different frequencies of PhPs propagate at different angles with respect to the z axis of the *h*-BN crystal. Equation (1) describes this correspondence: ^{31, 32}

$$\tan\theta(\omega)=i\frac{\sqrt{\varepsilon_t(\omega)}}{\sqrt{\varepsilon_z(\omega)}} \tag{1}$$
 where $\varepsilon_t(\omega)$ and $\varepsilon_z(\omega)$ are frequency-dependent dielectric functions of h -\$^{10}BN along in-plane and out-of-

where $\varepsilon_t(\omega)$ and $\varepsilon_z(\omega)$ are frequency-dependent dielectric functions of h^{-10} BN along in-plane and out-ofplane directions. Fig. 5a plots the propagation angle versus polariton energy. When PhP waves of different energy are launched by a point source, *i.e.*, the AFM tip, they traverse paths with different propagation angles and spatially separate. When two waves separate angularly and spatially, they do not interact, unless they meet again in space where conversion can happen.

Inspired by the standing wave conditions, we propose a possible energy transfer pathway from polaritons of ω_1 to polaritons of ω_2 that consists of a closed spatial propagation path starting from and returning to the tip. Firstly, the tip that is excited by IR pulses launches PhPs wave at ω_1 and traverse at a fixed angle of θ_1 . Then, the PhP wave propagates inside h- 10 BN to reach scattering sites that convert polaritons of ω_1 into *new* polaritons of ω_2 . The new polaritons of ω_2 propagate in all possible direction at the angle of θ_2 with respect to the z axis from the scattering site. When certain geometry constraints are satisfied, polaritons of ω_2 propagate back to the tip site and modifies the light matter interaction of subsequent IR pulses that contain ω_2 . The scattering sites of polaritons can be interfaces with defects or roughness. Or more likely, edges of the h- 10 BN flake, where both discontinuity and defects exist. Fig. 5b illustrates three possible configurations of propagation paths. If we consider material interfaces to be scattering sites, we can have polaritons of ω_1 to reflect integer times to reach a site at the interface where polaritons of ω_2 also behaves integer reflections. If we denote L as the distance between the tip and the scattering site, the number of bouncing segments of polariton wave l is determined by the tan θ to be $L = l \cdot \tan \theta$. Thus, to complete a closed path by polaritons of ω_1 and ω_2 , we arrived at the following Equation (2):

$$l_1 \cdot \tan \theta(\omega_1) = l_2 \cdot \tan \theta(\omega_2) \tag{2}$$

where l_1 and l_2 are positive integers representing the number of times that the polariton wave bounces inside h- 10 BN flake for ω_1 and ω_2 , respectively. Solving Equation (2) gives pairs of frequency (ω_1, ω_2) of polaritons that energy transfer can be detected. The spatial positioning of the interfacial scattering sites should be a ring of radius of L centered at the tip location. Moreover, interfacial scattering sites can also be located at concentric rings with radius being integer multiple of L. These sites represent additional configurations and satisfies Equation (2). In addition, when a scattering site is both at the interface and at the edge, its ability to convert polaritons of different energies should be greatly enhanced. This condition happens when the concentric rings of interfacial scattering sites intercept the flake edge. The top view panels of Fig 5b schematically illustrate such conditions. Note that there is also another configuration of pathway that could generate off-diagonal features, but it is unlikely to be the case for our measurement. The detailed discussion of this alternative is included in Supplementary Figure S7.

The positions of off-diagonal feature 5, 6, and 7 agree with Equation (2) of the above present model. Fig. 5c displays three plots of frequency pairs with $(l_1: l_2 = 2: 1)$, $(l_1: l_2 = 3: 1)$, and $(l_1: l_2 = 3: 2)$. Feature 5 represents energy transfer pathways from PhP modes around 1405 cm⁻¹ to PhP modes around

1427 cm⁻¹, which satisfies Equation (2) for $(l_1: l_2 = 2: 1)$ based on the dielectric functions of h^{-10} BN. Features 6 ($\omega_1 = 1405 \text{ cm}^{-1}$, $\omega_2 = 1470 \text{ cm}^{-1}$) satisfies the condition of $(l_1: l_2 = 3: 1)$ from Equation (2). Features 7 ($\omega_1 = 1440 \text{ cm}^{-1}$, $\omega_2 = 1470 \text{ cm}^{-1}$) meets the condition of $(l_1: l_2 = 3: 2)$. The reason why they are present in Fig. 4d, but absent in Fig. 4e is as follows: when the tip is closer to the edge, more effective edge scattering sites are closer and the polariton propagation losses are less. Moreover, standing wave cavity enhancement is present for $\omega_1 = 1440 \text{ cm}^{-1}$ when tip is 200 nm from the edge (Fig. 4d). The intrinsic stronger initial polaritons of ω_1 leads to more polaritons of ω_2 after energy transfer pathways. We have also performed measurement on natural h-BN. A similar off diagonal feature was observed and consistent with Equation (2) (see Supplementary Figure S8). Fig. 5d summarized the above discussed possible pathways for the generation of off-diagonal features in 2D PFIR spectra of h^{-10} BN.

The off-diagonal features of the AFM-2DIR spectra confirm energy transfer pathways from the PhP modes to the phonon mode, and the energy transfers between PhP modes. While energy transfers could occur in both directions, the dominant direction is from the collective modes with higher density of states to less populated, individual modes. The mismatch of the momentum in the polariton conversion could be compensated by the scattering process at the interfaces and edges; the difference in energy of tens of cm⁻¹ could come acoustic phonons from thermal energy of room temperature. Following this deduction, we should expect the upward energy transfer process among PhP modes to be significantly reduced when the thermal energy (k_BT) is smaller than the difference between PhP modes, a condition that may contribute to the long-range propagation of PhPs in *h*-BN under cryogenic temperature.

Discussion

The AFM-2DIR method would be uniquely suitable to study scientific questions involve IR energy transfer and mode coupling in nanoscale heterogeneous material and structures, where traditional 2DIR spectroscopy does not provide enough spatial precision. The applications include but not limited to spatially and spectrally studies of proteins secondary structures; 50-52 nano-phase separations of polymers, investigation of mode coupling between molecules and phononic/plasmonic structures; and phononic structures; and as under cryogenic temperatures. The ability to identify the anharmonicity and energy transfer of vibrational mode can also be beneficial for studying reactive molecule and intermediate of heterogeneous catalytical reactions. 56

Further improvement of the method may benefit from the utilization of a pulse shaper to generate ultra phase-stable pulse sequence at a faster scan speed than our stacked interferometer. A direct extension of this method may involve using four pulses for the excitation sequence, *i.e.*, the introduction of a wait time τ between t_1 and t_2 , to further decipher time-resolved energy transfer processes. Similar signal generation and detection mechanism should also be applicable for the visible frequency range, thus allowing *in situ* study of electronic transitions and energy transfers in photovoltaics.

Methods

Experimental setup and operation procedures of photothermal AFM-2DIR apparatus

The AFM-2DIR apparatus (Fig. 1a) consisted of three main components: the optical assembly for generating a femtosecond IR pulse sequence, an AFM with a metallic tip for field enhancement, and a signal extraction mechanism to register the photothermal signal. In our setup, femtosecond IR pulses of 200 fs duration were generated from the difference frequency generation (DFG) of an optical parametric amplifier (OPA, Orpheus with DFG II option, Light Conversion), pumped by a Yb:KGW amplifier (Pharos, Light Conversion) centered at 1030 nm of 190 fs duration. The IR beam was collinear with a He-Ne alignment laser to facilitate the beam alignment. The IR pulse sequence was generated from a compact assembly of

three Michelson interferometers with coated CaF_2 beam splitters (BSW511R, Thorlabs) built on a single piece of a temperature-regulated aluminum plate under an enclosure. The temperature of the interferometers was regulated by a PID controller (TC200, Thorlabs) connected to a resistive foil heater (HT10K, Thorlabs) underneath the aluminum plate. The temperature of the setpoint was ~1°C above the room temperature. The optical path of the interferometer arms was about 8 cm. The interferometer assembly created up to four independent time-delayed IR pulses from one IR input. Three of the IR pulses were used in our measurement. The relative timing between the first and second pulses was denoted as t_1 , scanned stepwise by a step motor (ZFS25B, Thorlabs). The timing between the second and third pulses was denoted as t_2 , which was scanned under the constant velocity mode by a direct-drive motor (DDMS100, Thorlabs). The output pulse sequence was guided into the tip-sample region of the AFM (Multimode 8, Bruker) with a parabolic mirror of 25 mm focal length.

We employed the signal extraction mechanism similar to the PFIR microscopy to collect the sample's photothermal signal from the tip-enhanced IR pulse sequence (Fig. 1b-d).²⁵ In PFIR operation, the AFM was operated under the peak force tapping (PFT) mode at 2 kHz. It was guided to a phase-locked loop (PLL) of a lock-in amplifier (MFLi-MF, Zurich Instrument). The output TTL from the PLL triggered a function generator (HDG2012B, Hantek) to generate a suitable trigger waveform for the laser emission of the Pharos laser amplifier. We adjusted the phase of the PLL so that the IR laser illumination was synchronized to the moment when the tip and the sample were in contact (Fig. 1b). A Pt-coated AFM tip (5 N/m, HQ:NSC/Pt 14, MikroMasch) was used. The highly localized light field induced the enhanced IR absorption from sample underneath the tip. The relaxation of IR absorption caused rapid thermal expansion of the sample surface within a microsecond. As a result, the expansion excited the tip and its cantilever to oscillate at hundreds of kHz shown in Fig. 1c. The cantilever's oscillations were read out through a built-in quadrant photodiode and sent to a digitizer (PXI-5122, National Instrument) with a data acquisition rate of 50 MHz and an average number of 64. The integrated amplitude of the cantilever oscillation after the FFT was registered as the photothermal signal S in Fig. 1d. We collected a series of interferograms by sequentially scanning the time delays of t₂ and t₁ and recorded the photothermal PFIR signal S. Fig. 1e displayed an interferogram by scanning t2 at constant velocity (15 µm/s) at a fixed t1. The scan range for t2 was set to 400 μm (beam traveled 800 μm). We scanned t₁ at a constant step size (500 nm/step) and collected corresponding interferograms from t_2 to form a two-dimensional interferogram $S(t_1, t_2)$. Sequential Fourier Transforms (FFTs) were applied to convert $S(t_1, t_2)$ into frequency domains $S(\omega_1, \omega_2)$.

Experimental setup of QCL-based PFIR microscope

Peak force infrared microscopy (PFIR) is a type of emerging AFM-IR technique with sub-10 nm spatialresolution. ²⁵ It was used to collect AFM-IR images from isotope-enriched hexagonal-boron nitride (h- 10 BN). The home-built PFIR setup consisted of a narrowband laser source (OCL: quantum cascade laser, MIRcat-QT, DRS Solutions), a Multimode AFM (Multimode 8, Bruker), a lock-in amplifier (MFLi-MF, Zurich Instrument), a function generator (HDG6122B, Hantek) and a data acquisition card (PXI-5122, National Instrument, operated at 50M samples per second). The AFM was operated under peak force tapping mode at 2 kHz. This frequency was routed to the lock-in amplifier and function generator to generate a train of transistor-to-transistor logic (TTL) waveforms as an external trigger for the QCL laser source. In this scheme, a single IR pulse (500 ns duration) illuminated the sample per one PFT cycle. The timing of the QCL output was adjusted and synchronized with every PFT cycle. The IR pulse was set to excite the tipsample region when the tip and sample were in contact. We guided the IR source to the side of the Pt-coated AFM tip (5 N/m, HQ:NSC/Pt 14, MikroMasch) by a parabolic mirror of 25 mm focal length. The photothermal expansion of the sample caused the AFM cantilever to oscillate, which was collected from the vertical deflection of a built-in photodiode of the AFM. We used a fourth-degree polynomial fitting to fit the slow-varying component of the vertical deflection signal due to the peak force tapping indentation. The fast oscillation signal from the photothermal expansion of the sample was obtained by subtracting the

vertical deflection signal with the fitted slow varying envelope for the polynomial fitting. Fast Fourier Transform (FFT) was applied to the subtracted vertical deflection signal waveform to convert the signal into the frequency domain. We integrated the amplitude across the mechanical resonance of the AFM cantilever in the FFTed signal in the frequency domain to obtain the PFIR signal. These calculations were executed in real time using a LabView program. We averaged 16 times to obtain one PFIR signal. The PFIR signal was routed to the AFM controller to be registered together with the AFM topography scan. The same AFM controller also registered the mechanical information from the PeakForce QNM (Quantitative Nanoscale Mechanical Characterization) function. To get the PFIR images from the h- 10 BN sample, we tuned the QCL to a range of wavenumbers from 1400 cm $^{-1}$ to 1440 cm $^{-1}$. Scanning parameters were set at an 8 μ m \times 8 μ m scan size across 512 \times 512 pixels, with a scan rate of 0.15 Hz per line to form the PFIR image.

Finite element simulations

Finite element simulation of the spatial distribution of the intensity of the IR field under Pt-coated tip. We calculated the IR field distribution of nano-gap between Pt tip and h-BN using commercial finite-difference time-domain (FDTD) simulation software (Lumerical Solutions, Inc). In our system, a Pt tip with a radius of 30 nm with a cone angle of 40 degrees was placed in 0.5 nm gap above a 40 nm thick h-BN on the Si substrate. As an excitation source for h-BN, a simplified monochromatic p-polarized IR field at 1400 cm⁻¹ with illumination angle of 10 degrees towards the h-BN surface was added. The simulated sectional profile of the EM field enhancement ratio is shown in Fig. 3h. The field enhancement ratio $|E/E_0|$ is defined as the ratio of field amplitude of the uniform incident IR field with the amplitude of the locally enhancement field.

Simulation of dispersion relation of PhP on h^{-10} BN. The dispersion model for simulation is the system of 40 nm thickness of h^{-10} BN on Si substrate in air. The simulation of dispersion relation of PhP on h^{-10} BN was done using the general oscillator (TO-LO form) based dielectric function formula³²:

$$\varepsilon_{\mu} = \varepsilon_{\infty\mu} \left(\frac{\omega_{LO,\mu}^2 - \omega^2 - i\Gamma_{\mu}\omega}{\omega_{TO,\mu}^2 - \omega^2 - i\Gamma_{\mu}\omega} \right), \quad \mu = \perp , //$$
(3)

where $\varepsilon_{\infty\mu}$ and Γ_{μ} are the high-frequency permittivity and the phonon damping, respectively. ω , $\omega_{LO,\mu}$ and $\omega_{TO,\mu}$ are the frequency, the LO and TO phonon frequencies. For our h^{-10} BN sample, we used 5.1 cm⁻¹ for $\varepsilon_{\infty\perp}$ and 2.5 cm⁻¹ for $\varepsilon_{\infty//}$. We took 1.8 cm⁻¹ for Γ_{\perp} and 1.0 cm⁻¹ for $\Gamma_{//}$. In the meantime, 1650 cm⁻¹, 845 cm⁻¹, 1394.5 cm⁻¹ and 785 cm⁻¹ were picked as $\omega_{LO,\perp}$, $\omega_{LO,//}$, $\omega_{TO,\perp}$ and $\omega_{TO,//}$, respectively.

The results from dielectric function above were then used to calculate the z-axis momentum of photon in h^{-10} BN layer k_e^{z} 6:

$$k_e^Z = \sqrt{\varepsilon_\perp \left(\frac{\omega^2}{c^2}\right) - \frac{\varepsilon_\perp}{\varepsilon_\parallel} q^2} \tag{4}$$

where c and q are the speed of light and momentum. With the dielectric constant of 1.0 and 12.0 for air and substrate, the z-axis momentum of photon was simulated through:

$$k_S^Z = \sqrt{\varepsilon_S \left(\frac{\omega^2}{c^2}\right) - q^2}$$

$$k_a^Z = \sqrt{\varepsilon_a \left(\frac{\omega^2}{c^2}\right) - q^2}$$
(5)

Then, to find the complex reflectivity r_p , we put this z-axis momentum calculated form our system to the equations below:

$$r_{S} = \frac{\varepsilon_{S} k_{e}^{Z} - \varepsilon_{\perp} k_{S}^{Z}}{\varepsilon_{S} k_{e}^{Z} + \varepsilon_{\perp} k_{S}^{Z}}$$

$$r_{a} = \frac{\varepsilon_{\perp} k_{a}^{Z} - \varepsilon_{a} k_{e}^{Z}}{\varepsilon_{\perp} k_{a}^{Z} + \varepsilon_{a} k_{e}^{Z}}$$

$$r_{p} = \frac{r_{a} + r_{S} e^{2idk_{e}^{Z}}}{1 + r_{a} r_{S} e^{2idk_{e}^{Z}}}$$
(6)

And the simulated result from MATLAB is plotted in Fig. 3i with the grey scale bar on the right.

Sample preparation

PMMA-N₃ film. The polymer film was prepared by spin-coating 20 μ L 20 mg/mL ω -azide-terminated polymethyl methacrylate (P41623-MA-N₃, Polymer Source, MW: 1000) shortened as PMMA-N₃ in toluene solvent on silicon surface. The spin coater was set to 300 rpm for 15 s and 1500 rpm for 50 s.

h-¹⁰BN fabrication and preparation. The synthesis of h-¹⁰BN followed a method reported by Liu $et~al^{46}$ and consisted of two steps: ingot formation and crystal growth. In the ingot formation step, an alumina boat was filled with powdered boron and metal. 2.15 wt% ¹⁰B with balance iron with a total mass of 50 g was used. The alumina boat was put in an alumina tube furnace with a nitrogen purge to remove oxygen, and then a N₂/H₂ mixture with 11% H₂ is flowed through the tube for the duration of the experiment. The furnace was heated to 1550°C and maintained for 24 hours to ensure the materials melted and mixed well. Afterward, the system is quenched to form an ingot. In the crystal growth step, the ingot was purged with nitrogen, then held the furnace at 1550°C for 24 hours with the same N₂/H₂ mixture. Afterward, the furnace was slowly cooled at 1°C/hour to cause h-BN to precipitate. Once the furnace reached 1500°C, it is quenched. The resulting ingot was covered in a thin layer of h-¹⁰BN crystals and peeled off for usage. The h-¹⁰BN thin films on Si substrate were prepared by exfoliation using Scotch tape. The thickness of the h-¹⁰BN flake was found to be ~40 nm (Supplementary Fig. S3).

Author Contributions

X.G.X conceived the design of the AFM-2DIR experiment and instrument. The experimental setup was built by X.G.X. and Q.X. Q.X. carried out the experiment, simulation, and data collection. E. J. and J.H.E. provides the isotope-enriched h- 10 BN for the study. Y. Z. provided assistance on the carbonyl anharmonicity interpretation. The manuscript was written together by X.G.X. and Q.X. X.G.X. oversaw the research.

Acknowledgement

We would like to thank Dr. Martin Zanni, Dr. Gilbert Walker, Dr. Jian-Hua Jiang, and Dr. John T. King for encouragement and consultation on the 2DIR spectroscopy or time-resolved spectroscopy. X. G. X. would like to thank the support from Beckman Young Investigator Award from the Arnold and Mabel Beckman Foundation, the Sloan Research Fellowship from the Alfred P. Sloan Foundation, and the Camille Dreyfus Teacher-Scholar Award from the Camille and Henry Dreyfus Foundation. Q.X. and X. G. X. would also like to thank the support from the National Science Foundation, award number CHE 1847765. Support for the *h*-BN crystal growth came from the Office of Naval Research, award number N00014-22-1-2582.

References:

- 1. Chen, X.; Hu, D.; Mescall, R.; You, G.; Basov, D. N.; Dai, Q.; Liu, M., Modern scattering-type scanning near-field optical microscopy for advanced material research. *Advanced Materials* **2019**, *31* (24), 1804774.
- 2. Hillenbrand, R.; Taubner, T.; Keilmann, F., Phonon-enhanced light–matter interaction at the nanometre scale. *Nature* **2002**, *418* (6894), 159-162.
- 3. Qazilbash, M. M.; Brehm, M.; Chae, B.-G.; Ho, P. C.; Andreev, G. O.; Kim, B.-J.; Yun, S. J.; Balatsky, A. V.; Maple, M. B.; Keilmann, F., Mott transition in VO2 revealed by infrared spectroscopy and nano-imaging. *Science* **2007**, *318* (5857), 1750-1753.
- 4. Mathurin, J.; Deniset-Besseau, A.; Bazin, D.; Dartois, E.; Wagner, M.; Dazzi, A., Photothermal AFM-IR spectroscopy and imaging: Status, challenges, and trends. *Journal of Applied Physics* **2022**, *131* (1).
- 5. Basov, D. N.; Fogler, M. M.; García de Abajo, F. J., Polaritons in van der Waals materials. *Science* **2016**, *354* (6309), aag1992.
- 6. Dai, S.; Fei, Z.; Ma, Q.; Rodin, A. S.; Wagner, M.; McLeod, A. S.; Liu, M. K.; Gannett, W.; Regan, W.; Watanabe, K.; Taniguchi, T.; Thiemens, M.; Dominguez, G.; Neto, A. H. C.; Zettl, A.; Keilmann, F.; Jarillo-Herrero, P.; Fogler, M. M.; Basov, D. N., Tunable Phonon Polaritons in Atomically Thin van der Waals Crystals of Boron Nitride. *Science* **2014**, *343* (6175), 1125-1129.
- 7. Xu, X. G.; Ghamsari, B. G.; Jiang, J.-H.; Gilburd, L.; Andreev, G. O.; Zhi, C.; Bando, Y.; Golberg, D.; Berini, P.; Walker, G. C., One-dimensional surface phonon polaritons in boron nitride nanotubes. *Nature Communications* **2014**, *5* (1), 4782.
- 8. Hu, G.; Ou, Q.; Si, G.; Wu, Y.; Wu, J.; Dai, Z.; Krasnok, A.; Mazor, Y.; Zhang, Q.; Bao, Q., Topological polaritons and photonic magic angles in twisted α-MoO₃ bilayers. *Nature* **2020**, *582* (7811), 209-213.
- 9. Luo, C.; Guo, X.; Hu, H.; Hu, D.; Wu, C.; Yang, X.; Dai, Q., Probing polaritons in 2D materials. *Advanced Optical Materials* **2020**, *8* (5), 1901416.
- 10. Tamagnone, M.; Ambrosio, A.; Chaudhary, K.; Jauregui, L. A.; Kim, P.; Wilson, W. L.; Capasso, F., Ultra-confined mid-infrared resonant phonon polaritons in van der Waals nanostructures. *Science Advances* **2018**, *4* (6), eaat7189.
- 11. Schwartz, J. J.; Jakob, D. S.; Centrone, A., A guide to nanoscale IR spectroscopy: resonance enhanced transduction in contact and tapping mode AFM-IR. *Chemical Society Reviews* **2022**, *51* (13), 5248-5267.
- 12. Wang, L.; Wagner, M.; Wang, H.; Pau-Sanchez, S.; Li, J.; Edgar, J. H.; Xu, X. G., Revealing phonon polaritons in hexagonal boron nitride by multipulse peak force infrared microscopy. *Advanced Optical Materials* **2020**, *8* (5), 1901084.
- 13. Hamm, P.; Lim, M.; Hochstrasser, R. M., Structure of the amide I band of peptides measured by femtosecond nonlinear-infrared spectroscopy. *The Journal of Physical Chemistry B* **1998**, *102* (31), 6123-6138.
- 14. Hamm, P.; Lim, M.; DeGrado, W. F.; Hochstrasser, R. M., The two-dimensional IR nonlinear spectroscopy of a cyclic penta-peptide in relation to its three-dimensional structure. *Proceedings of the National Academy of Sciences* **1999**, *96* (5), 2036-2041.
- 15. Khalil, M.; Demirdöven, N.; Tokmakoff, A., Coherent 2D IR Spectroscopy: Molecular Structure and Dynamics in Solution. *The Journal of Physical Chemistry A* **2003**, *107* (27), 5258-5279.

- 16. Asplund, M. C.; Zanni, M. T.; Hochstrasser, R. M., Two-dimensional infrared spectroscopy of peptides by phase-controlled femtosecond vibrational photon echoes. *Proceedings of the National Academy of Sciences* **2000**, *97* (15), 8219-8224.
- 17. Zheng, J.; Kwak, K.; Fayer, M. D., Ultrafast 2D IR vibrational echo spectroscopy. *Accounts of Chemical Research* **2007**, *40* (1), 75-83.
- 18. Wagner, M.; Fei, Z.; McLeod, A. S.; Rodin, A. S.; Bao, W.; Iwinski, E. G.; Zhao, Z.; Goldflam, M.; Liu, M.; Dominguez, G., Ultrafast and nanoscale plasmonic phenomena in exfoliated graphene revealed by infrared pump–probe nanoscopy. *Nano Letters* **2014**, *14* (2), 894-900.
- 19. Yao, Z.; Xu, S.; Hu, D.; Chen, X.; Dai, Q.; Liu, M., Nanoimaging and nanospectroscopy of polaritons with time resolved s-SNOM. *Advanced Optical Materials* **2020**, *8* (5), 1901042.
- Wagner, M.; McLeod, A. S.; Maddox, S. J.; Fei, Z.; Liu, M.; Averitt, R. D.; Fogler, M. M.; Bank, S. R.; Keilmann, F.; Basov, D. N., Ultrafast Dynamics of Surface Plasmons in InAs by Time-Resolved Infrared Nanospectroscopy. *Nano Letters* 2014, *14* (8), 4529-4534.
- 21. Yoxall, E.; Schnell, M.; Nikitin, A. Y.; Txoperena, O.; Woessner, A.; Lundeberg, M. B.; Casanova, F.; Hueso, L. E.; Koppens, F. H. L.; Hillenbrand, R., Direct observation of ultraslow hyperbolic polariton propagation with negative phase velocity. *Nature Photonics* **2015**, *9* (10), 674-678.
- 22. Zhang, X.; Yan, Q.; Ma, W.; Zhang, T.; Yang, X.; Zhang, X.; Li, P., Ultrafast anisotropic dynamics of hyperbolic nanolight pulse propagation. *Science Advances* **2023**, *9* (34), eadi4407.
- 23. Eisele, M.; Cocker, T. L.; Huber, M. A.; Plankl, M.; Viti, L.; Ercolani, D.; Sorba, L.; Vitiello, M. S.; Huber, R., Ultrafast multi-terahertz nano-spectroscopy with sub-cycle temporal resolution. *Nature Photonics* **2014**, *8* (11), 841-845.
- 24. Jiang, T.; Kravtsov, V.; Tokman, M.; Belyanin, A.; Raschke, M. B., Ultrafast coherent nonlinear nanooptics and nanoimaging of graphene. *Nature Nanotechnology* **2019**, *14* (9), 838-843.
- 25. Wang, L.; Wang, H.; Xu, X. G., Principle and applications of peak force infrared microscopy. *Chemical Society Reviews* **2022**, *51* (13), 5268-5286.
- 26. Schneider, S. H.; Kratochvil, H. T.; Zanni, M. T.; Boxer, S. G., Solvent-Independent Anharmonicity for Carbonyl Oscillators. *The Journal of Physical Chemistry B* **2017**, *121* (10), 2331-2338.
- 27. Wang, H.; Xie, Q.; Zhang, Y.; Xu, X. G., Photothermally Probing Vibrational Excited-State Absorption with Nanoscale Spatial Resolution through Frequency-Domain Pump-Probe Peak Force Infrared Microscopy. *The Journal of Physical Chemistry C* **2021**, *125* (15), 8333-8338.
- 28. Caldwell, J. D.; Kretinin, A. V.; Chen, Y.; Giannini, V.; Fogler, M. M.; Francescato, Y.; Ellis, C. T.; Tischler, J. G.; Woods, C. R.; Giles, A. J.; Hong, M.; Watanabe, K.; Taniguchi, T.; Maier, S. A.; Novoselov, K. S., Sub-diffractional volume-confined polaritons in the natural hyperbolic material hexagonal boron nitride. *Nature Communications* **2014**, *5* (1), 5221.
- 29. Li, N.; Guo, X.; Yang, X.; Qi, R.; Qiao, T.; Li, Y.; Shi, R.; Li, Y.; Liu, K.; Xu, Z.; Liu, L.; García de Abajo, F. J.; Dai, Q.; Wang, E.-G.; Gao, P., Direct observation of highly confined phonon polaritons in suspended monolayer hexagonal boron nitride. *Nature Materials* **2021**, *20* (1), 43-48.

- 30. Li, P.; Lewin, M.; Kretinin, A. V.; Caldwell, J. D.; Novoselov, K. S.; Taniguchi, T.; Watanabe, K.; Gaussmann, F.; Taubner, T., Hyperbolic phonon-polaritons in boron nitride for near-field optical imaging and focusing. *Nature Communications* **2015**, *6* (1), 7507.
- 31. Dai, S.; Ma, Q.; Andersen, T.; McLeod, A. S.; Fei, Z.; Liu, M. K.; Wagner, M.; Watanabe, K.; Taniguchi, T.; Thiemens, M.; Keilmann, F.; Jarillo-Herrero, P.; Fogler, M. M.; Basov, D. N., Subdiffractional focusing and guiding of polaritonic rays in a natural hyperbolic material. *Nature Communications* **2015**, *6* (1), 6963.
- 32. Giles, A. J.; Dai, S.; Vurgaftman, I.; Hoffman, T.; Liu, S.; Lindsay, L.; Ellis, C. T.; Assefa, N.; Chatzakis, I.; Reinecke, T. L.; Tischler, J. G.; Fogler, M. M.; Edgar, J. H.; Basov, D. N.; Caldwell, J. D., Ultralow-loss polaritons in isotopically pure boron nitride. *Nature Materials* **2018**, *17* (2), 134-139.
- 33. Caldwell, J. D.; Aharonovich, I.; Cassabois, G.; Edgar, J. H.; Gil, B.; Basov, D. N., Photonics with hexagonal boron nitride. *Nature Reviews Materials* **2019**, *4* (8), 552-567.
- 34. Alfaro-Mozaz, F. J.; Rodrigo, S. G.; Vélez, S.; Dolado, I.; Govyadinov, A.; Alonso-González, P.; Casanova, F.; Hueso, L. E.; Martín-Moreno, L.; Hillenbrand, R.; Nikitin, A. Y., Hyperspectral Nanoimaging of van der Waals Polaritonic Crystals. *Nano Letters* **2021**, *21* (17), 7109-7115.
- 35. Alfaro-Mozaz, F. J.; Alonso-González, P.; Vélez, S.; Dolado, I.; Autore, M.; Mastel, S.; Casanova, F.; Hueso, L. E.; Li, P.; Nikitin, A. Y.; Hillenbrand, R., Nanoimaging of resonating hyperbolic polaritons in linear boron nitride antennas. *Nature Communications* **2017**, *8* (1), 15624.
- 36. Chaudhary, K.; Tamagnone, M.; Rezaee, M.; Bediako, D. K.; Ambrosio, A.; Kim, P.; Capasso, F., Engineering phonon polaritons in van der Waals heterostructures to enhance inplane optical anisotropy. *Science Advances* 5 (4), eaau7171.
- 37. Wang, L.; Wagner, M.; Wang, H.; Pau-Sanchez, S.; Li, J.; Edgar, J. H.; Xu, X. G., Revealing Phonon Polaritons in Hexagonal Boron Nitride by Multipulse Peak Force Infrared Microscopy. *Advanced Optical Materials* **2020**, *8* (5), 1901084.
- 38. Yang, Y.; Finch, M. F.; Xiong, D.; Lail, B. A., Hybrid long-range hyperbolic phonon polariton waveguide using hexagonal boron nitride for mid-infrared subwavelength confinement. *Opt. Express* **2018**, *26* (20), 26272-26282.
- 39. Autore, M.; Li, P.; Dolado, I.; Alfaro-Mozaz, F. J.; Esteban, R.; Atxabal, A.; Casanova, F.; Hueso, L. E.; Alonso-González, P.; Aizpurua, J.; Nikitin, A. Y.; Vélez, S.; Hillenbrand, R., Boron nitride nanoresonators for phonon-enhanced molecular vibrational spectroscopy at the strong coupling limit. *Light: Science & Applications* **2018**, *7* (4), 17172-17172.
- 40. Klemens, P. G., Anharmonic Decay of Optical Phonons. *Physical Review* **1966**, *148* (2), 845-848.
- 41. Srivastava, G. P., The anharmonic phonon decay rate in group-III nitrides. *Journal of Physics: Condensed Matter* **2009**, *21* (17), 174205.
- 42. Cuscó, R.; Artús, L.; Edgar, J. H.; Liu, S.; Cassabois, G.; Gil, B., Isotopic effects on phonon anharmonicity in layered van der Waals crystals: Isotopically pure hexagonal boron nitride. *Physical Review B* **2018**, *97* (15), 155435.
- 43. Ni, G.; McLeod, A. S.; Sun, Z.; Matson, J. R.; Lo, C. F. B.; Rhodes, D. A.; Ruta, F. L.; Moore, S. L.; Vitalone, R. A.; Cusco, R., Long-lived phonon polaritons in hyperbolic materials. *Nano Letters* **2021**, *21* (13), 5767-5773.

- 44. Lee, I.-H.; He, M.; Zhang, X.; Luo, Y.; Liu, S.; Edgar, J. H.; Wang, K.; Avouris, P.; Low, T.; Caldwell, J. D.; Oh, S.-H., Image polaritons in boron nitride for extreme polariton confinement with low losses. *Nature Communications* **2020**, *11* (1), 3649.
- 45. Wang, H.; Janzen, E.; Wang, L.; Edgar, J. H.; Xu, X. G., Probing mid-infrared phonon polaritons in the aqueous phase. *Nano Letters* **2020**, *20* (5), 3986-3991.
- 46. Liu, S.; He, R.; Xue, L.; Li, J.; Liu, B.; Edgar, J. H., Single crystal growth of millimeter-sized monoisotopic hexagonal boron nitride. *Chemistry of Materials* **2018**, *30* (18), 6222-6225.
- 47. Xie, Q.; Xu, X. G., Fourier-Transform Atomic Force Microscope-Based Photothermal Infrared Spectroscopy with Broadband Source. *Nano Letters* **2022**, *22* (22), 9174-9180.
- 48. Hamm, P.; Zanni, M., *Concepts and methods of 2D infrared spectroscopy*. Cambridge University Press: 2011.
- 49. Ni, G.; McLeod, A. S.; Sun, Z.; Matson, J. R.; Lo, C. F. B.; Rhodes, D. A.; Ruta, F. L.; Moore, S. L.; Vitalone, R. A.; Cusco, R.; Artús, L.; Xiong, L.; Dean, C. R.; Hone, J. C.; Millis, A. J.; Fogler, M. M.; Edgar, J. H.; Caldwell, J. D.; Basov, D. N., Long-Lived Phonon Polaritons in Hyperbolic Materials. *Nano Letters* **2021**, *21* (13), 5767-5773.
- 50. Ruggeri, F. S.; Mannini, B.; Schmid, R.; Vendruscolo, M.; Knowles, T. P. J., Single molecule secondary structure determination of proteins through infrared absorption nanospectroscopy. *Nature Communications* **2020**, *11* (1), 2945.
- 51. Middleton, C. T.; Woys, A. M.; Mukherjee, S. S.; Zanni, M. T., Residue-specific structural kinetics of proteins through the union of isotope labeling, mid-IR pulse shaping, and coherent 2D IR spectroscopy. *Methods* **2010**, *52* (1), 12-22.
- 52. Shim, S.-H.; Strasfeld, D. B.; Ling, Y. L.; Zanni, M. T., Automated 2D IR spectroscopy using a mid-IR pulse shaper and application of this technology to the human islet amyloid polypeptide. *Proceedings of the National Academy of Sciences* **2007**, *104* (36), 14197-14202.
- 53. Dolado, I.; Maciel-Escudero, C.; Nikulina, E.; Modin, E.; Calavalle, F.; Chen, S.; Bylinkin, A.; Alfaro-Mozaz, F. J.; Li, J.; Edgar, J. H.; Casanova, F.; Vélez, S.; Hueso, L. E.; Esteban, R.; Aizpurua, J.; Hillenbrand, R., Remote near-field spectroscopy of vibrational strong coupling between organic molecules and phononic nanoresonators. *Nature Communications* **2022**, *13* (1), 6850.
- 54. Guo, X.; Li, N.; Yang, X.; Qi, R.; Wu, C.; Shi, R.; Li, Y.; Huang, Y.; García de Abajo, F. J.; Wang, E.-G., Hyperbolic whispering-gallery phonon polaritons in boron nitride nanotubes. *Nature Nanotechnology* **2023**, 1-6.
- 55. Ni, G. X.; McLeod, A. S.; Sun, Z.; Wang, L.; Xiong, L.; Post, K. W.; Sunku, S. S.; Jiang, B. Y.; Hone, J.; Dean, C. R.; Fogler, M. M.; Basov, D. N., Fundamental limits to graphene plasmonics. *Nature* **2018**, *557* (7706), 530-533.
- 56. Dery, S.; Gross, E., IR Nanospectroscopy in Catalysis Research. In *Ambient Pressure Spectroscopy in Complex Chemical Environments*, American Chemical Society: 2021; Vol. 1396, pp 147-173.

Figures

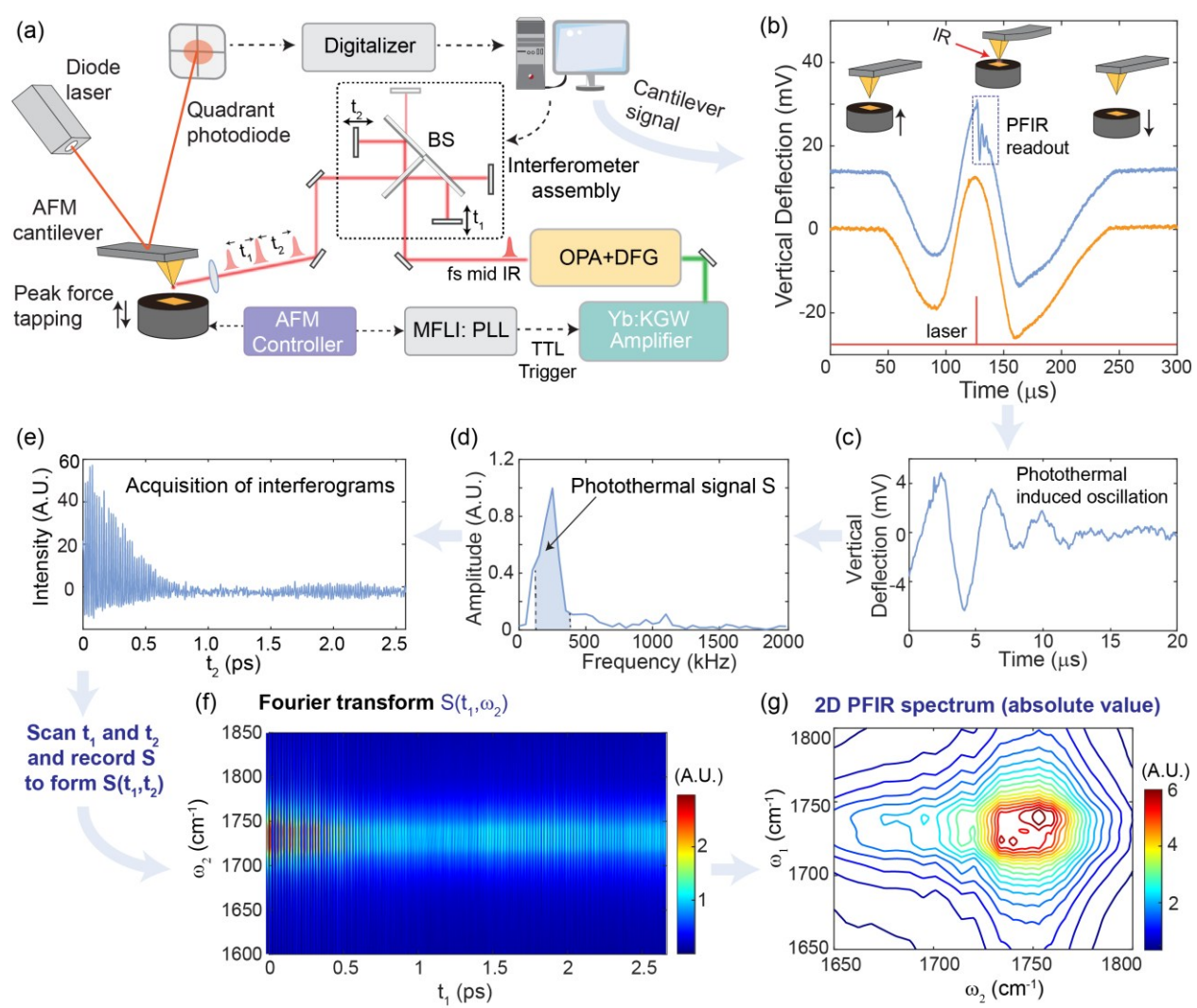


Fig. 1 Operation flow of the AFM-2DIR method with the PFIR detection. (a) Schematics of the experimental apparatus. (b) Vertical deflection signals of the AFM cantilever with (blue) and without (orange) laser illuminations. The IR pulse sequence arrives when the tip and sample are in contact. The additional cantilever oscillations are due to sample's photothermal expansion (dashed box). (c) The extracted photothermal induced oscillation after removing the slow varying curvature of the AFM cantilever through polynomial fitting (at the 4th order). (d) Fourier transformation of the extracted cantilever oscillations. The area across the mechanical resonance is integrated and used as the photothermal signal *S*. (e) Interferograms are collected by fast scanning the time delay t_2 at each t_1 step. The response is from carbonyl mode of a PMMA-N₃ polymer thin film. (f) The spectrogram obtained from Fourier transform of the interferogram along t_2 into the frequency domain $ω_2$ under each t_1 . (g) 2D PFIR spectrum obtained from subsequent Fourier transform on t_1 . The absolute value of the 2D spectrum is shown here.

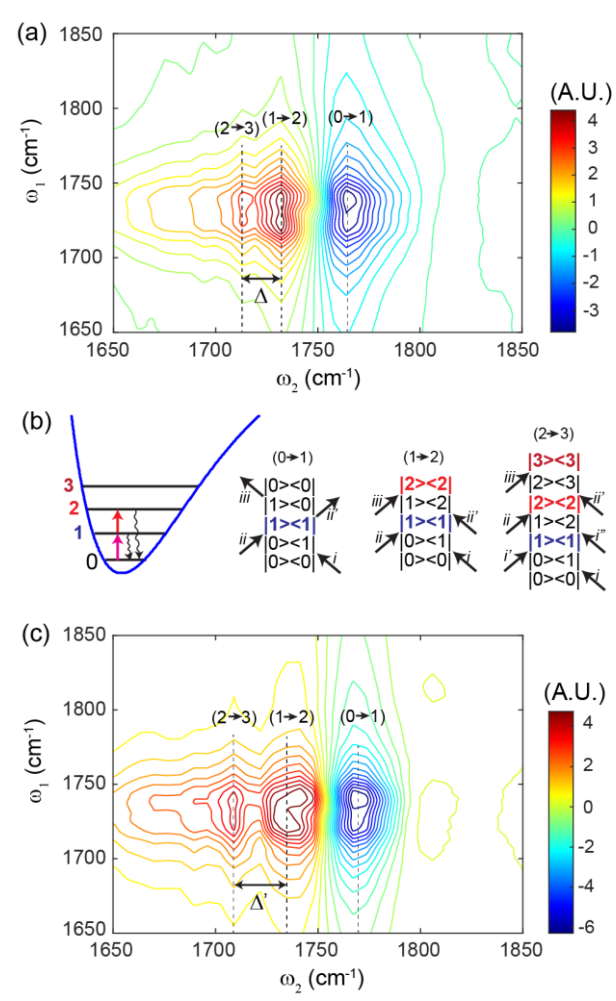


Fig. 2 Representations of 2D PFIR spectrum of carbonyl vibrational mode. (a) The real part plot of the 2D PFIR spectrum. The double-sided arrow marks the anharmonicity $\Delta = 19 \text{ cm}^{-1}$, estimated from the spacing from the overtone absorptions. (b) Vibrational potential energy surface (PES) and three representative Feynmann diagram pathways related to the 2D PFIR spectroscopic features of carbonyl vibrational mode. (c) The real part plot of the 2D PFIR spectrum under 25% more IR intensity than that of (a). The spectrum in (c) shows a slight blueshift of 4 cm⁻¹ of (0 \rightarrow 1), and an increase anharmonicity Δ ', which is found to be 26 cm⁻¹.

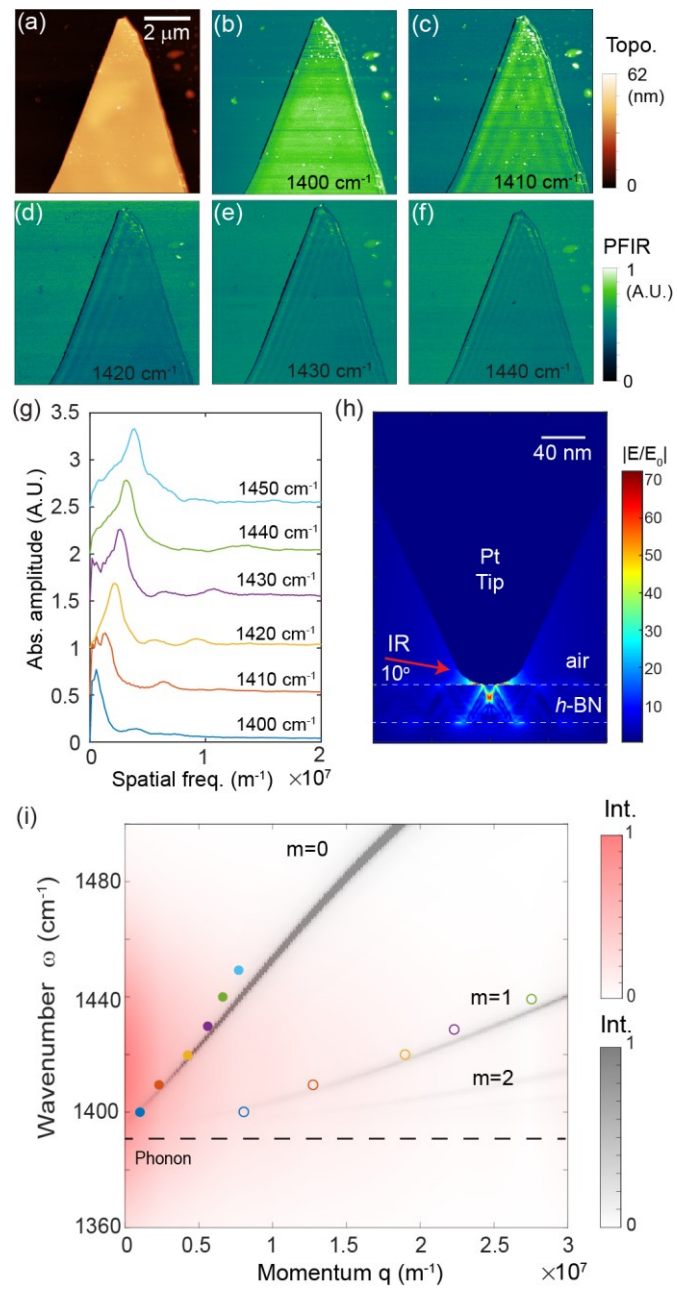


Fig. 3 Real space mapping and interpretation of HPhP of a h- 10 BN flake. (a) AFM topography of an h- 10 BN flake. (b-f) The PFIR images of the same flake under narrowband QCL IR illuminations from 1400 cm $^{-1}$ to 1440 cm $^{-1}$ with 10 cm $^{-1}$ increment, showing interference fringes. (g) Extraction of the spatial frequencies of the interference fringes from PFIR measurement at different IR frequencies. The plots are vertically offset for clarity. (h) Finite element simulation of the spatial distribution of the field enhancement ratio of the IR field. The IR frequency was set at 1400 cm $^{-1}$; the illumination angle was set at 10 degrees; tip radius was chosen at 30 nm; the tip cone angle was 40 degree. (i) The overlap of simulated dispersion relation of PhP with the bandwidths of the IR radiation of the IR source and available momentum from the finite element simulation in (h). The orders of the PhP modes are denoted as m = 0, 1, 2. The phonon position is marked by a horizontal dashed line. The experimentally extracted momenta versus IR frequencies from the peaks of (g) are plotted on top of the dispersion relation of m = 0 (colored filled dot) and m = 1 (colored circles).

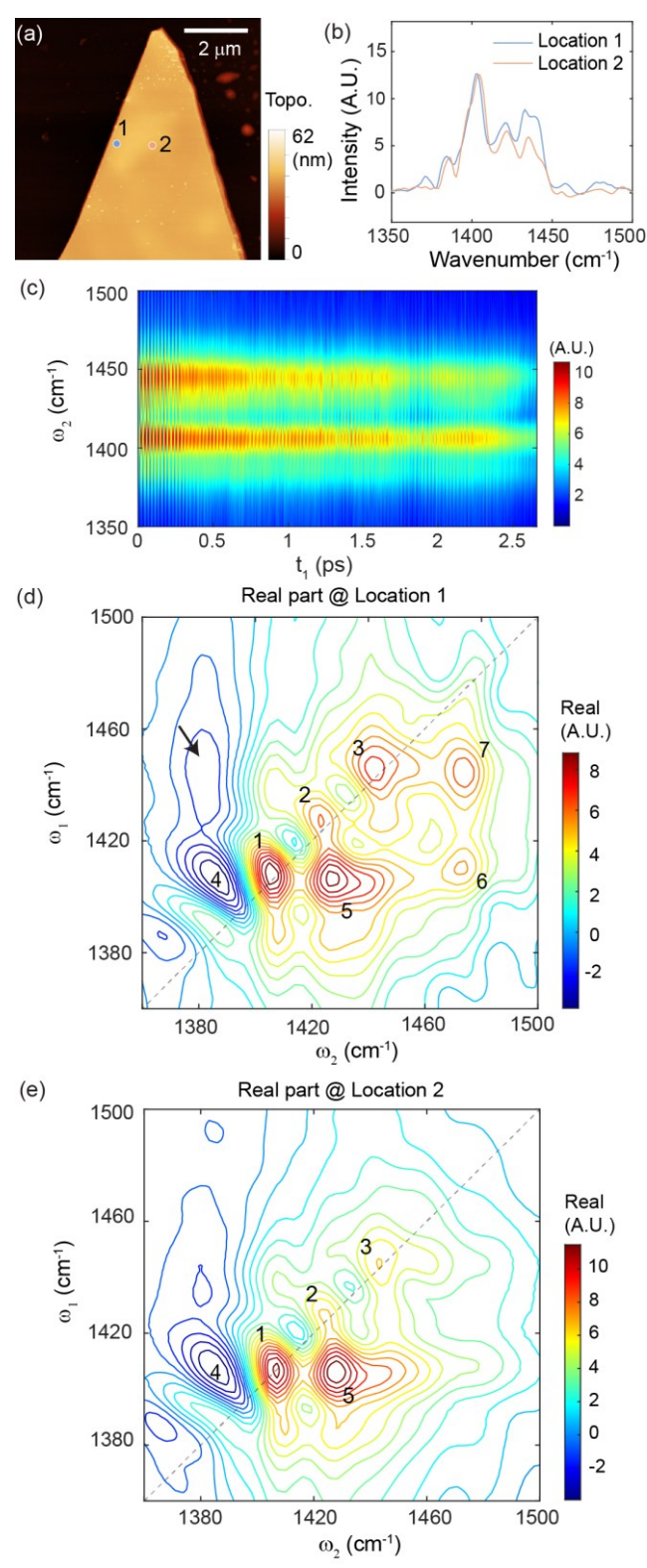


Fig. 4 2D PFIR spectra of h-¹⁰BN revealing energy transfers. (a) Topography of the h-¹⁰BN flake. Two measurement locations are marked by Location 1 and Location 2. (b) FT-PFIR spectra of Location 1 in blue and Location 2 in orange. (c) Spectrogram $S(t_1, \omega_2)$ after FFT along t_2 of the measured interferograms from Location 1. (d) The real part of the 2D PFIR spectrum from Location 1. (e) The real part of the 2D PFIR spectrum from Location 2. The dashed lines in (d) and (e) indicate the diagonal direction.

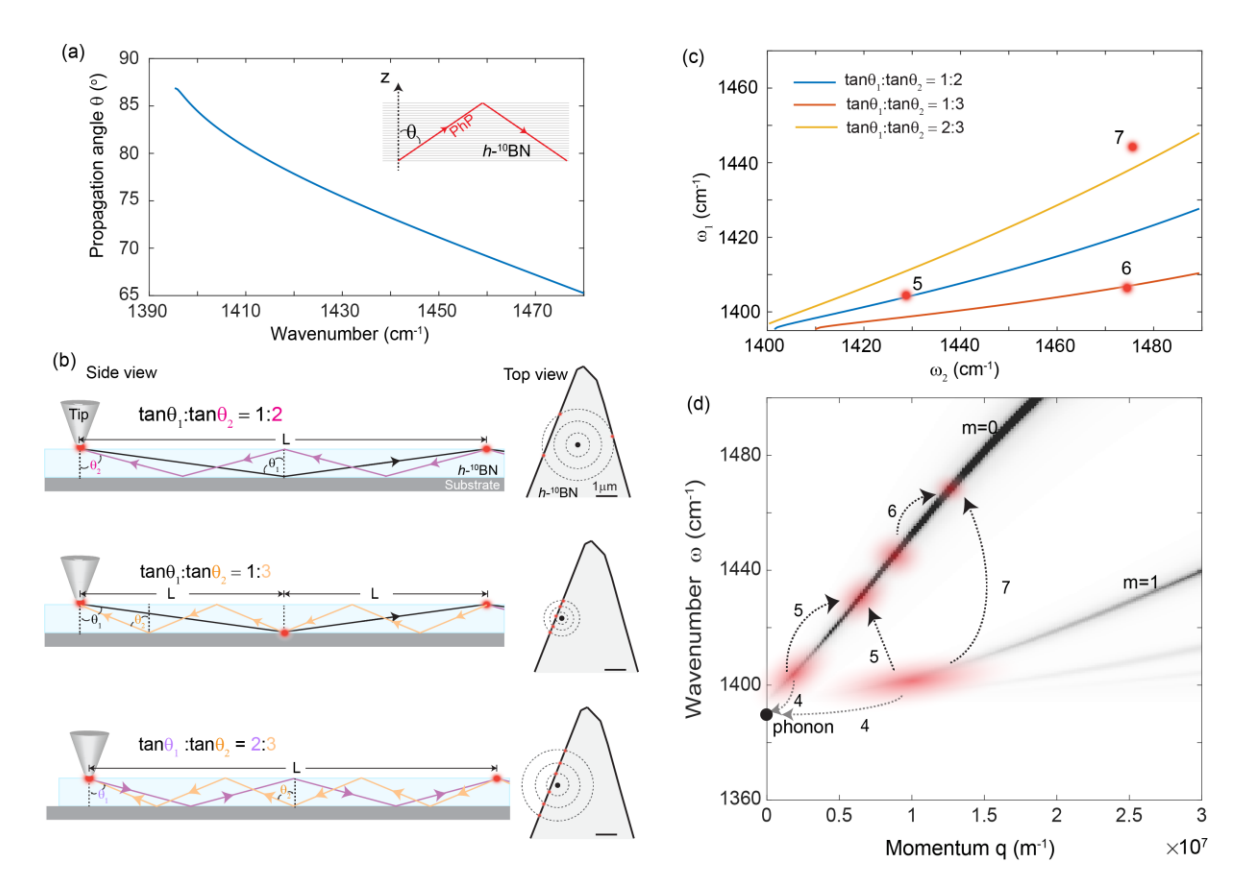


Fig. 5 PhP propagation characteristics in h^{-10} BN and energy transfer pathways. (a) The relationship between polariton IR energy (ω in cm⁻¹) and the propagation angle θ versus the z-axis of the h-BN crystal. (b) Schematic representations of three possible PhP propagation and conversion pathways that the newly generated PhP propagates back to the tip position. From the side views, the potential scattering site and the tip launching site are marked by red dots. Their paths are connected by two polariton waves propagates at angles θ_1 and θ_2 , each with integer number of reflections within the h^{-10} BN flake. The length between the tip launching site and the potential scattering site is marked as L. From the top views. The tip launch sites are marked by black dots, and the potential scattering sites form a series of concentric rings with radius of L, 2L, 3L, etc. When the rings intercept the flake edge, the scattering ability is greatly enhanced. Red dots mark these intercepts. (c) Calculated relationships between ω_1 and ω_2 that satisfy the requirements described by Equation (2). Three red dots correspond to the off-diagonal features 5, 6, and 7. (d) A summary of the energy transfer pathways of the off-diagonal features 4-7 in Fig. 4d.